MOLECULAR SIGNATURES IN THE NEAR-INFRARED DAYSIDE SPECTRUM OF HD 189733b

M. R. Swain[1], G. Vasisht[1], G. Tinetti[2], J. Bouwman[3], Pin Chen[1], Y. Yung[4], D. Deming[5], and P. Deroo[1]
[1] Jet Propulsion Laboratory California, Institute of Technology, 4800 Oak Grove Drive, Pasadena, CA 91109, USA
[2] University College London, Gower Street, London WC1E 6BT, UK
[3] Max-Planck Institute for Astronomy, Konigstuhl 17, D-69117 Heidelberg, Germany
[4] Division of Geological and Planetary Sciences, California Institute of Technology, Pasadena, CA 91125, USA
[5] Goddard Space Flight Center, Planetary Systems Branch, Code 693, Greenbelt, MD, USA

ABSTRACT

We have measured the dayside spectrum of HD 189733b between 1.5 and 2.5 μm using the NICMOS instrument on the *Hubble Space Telescope*. The emergent spectrum contains significant modulation, which we attribute to the presence of molecular bands seen in absorption. We find that water (H_2O), carbon monoxide (CO), and carbon dioxide (CO_2) are needed to explain the observations, and we are able to estimate the mixing ratios for these molecules. We also find temperature decreases with altitude in the $\sim 0.01 < P < \sim 1$ bar region of the dayside near-infrared photosphere and set an upper limit to the dayside abundance of methane (CH_4) at these pressures.

Key words: planetary systems – techniques: spectroscopic

1. INTRODUCTION

HD 189733b is a transiting hot-Jupiter planet in a 2.2 day orbit around a K2V stellar primary (Bouchy et al. 2005). Due to the relatively large depth of the eclipse ($\sim 2.5\%$ at K band) and the bright stellar primary (Kmag = 5.5), this system was immediately recognized as an important target for atmospheric characterization observations, and its emission has been studied extensively during secondary eclipse (Deming et al. 2005; Knutson et al. 2007; Grillmair et al. 2007; Knutson et al. 2008; Charbonneau et al. 2008). Multicolor photometric observations revealed the presence of H_2O (Tinetti et al. 2007a) and the likely presence of CO (Charbonneau et al. 2008), while optical transmission spectroscopy suggests scattering by high-altitude haze (Pont et al. 2008). In addition, extensive theoretical work has also been done on the atmosphere of this planet by Fortney et al. (2006); Barman (2008); Burrows et al. (2008); Showman et al. (2008), and others.

Recently, the NICMOS camera on the *Hubble Space Telescope (HST)* was used during the primary eclipse of HD 189733b to obtain a near-IR transmission spectrum of the planet's atmosphere; these results showed the presence of H_2O and CH_4 (Swain et al. 2008; hereafter SVT08). The near-IR transmission spectrum of HD 189733b probes the upper ($P \sim 10^{-4}$ bar estimated from our models) regions of the atmosphere at the terminator. In this Letter, we report the results of *HST* observations of the dayside spectrum (derived from secondary eclipse measurements). At near-IR wavelengths, the dayside portion of the atmosphere of HD 189433b is probed in deeper ($P \sim 0.1$ bar estimated from our models) regions.

2. OBSERVATIONS

We observed HD 189733 with the *HST* for five contiguous spacecraft orbits, using NICMOS in imaging-spectroscopy mode with the G206 grism (wavelength coverage 1.4–2.5 μm). Observations began on 2007 April 29 at UT 23:47:58 and ended at UT 06:51:52 on the next day. The first two orbits (O_1 & O_2) observed the target pre-ingress, the third orbit (O_3) was phased to capture the occultation, while the fourth and fifth orbits (O_4 & O_5) were post-egress (see Figure 1). A total of 638 usable snapshot spectra were acquired during the five orbits. The third

orbit (the occultation) contained 130 spectra. Using the best available ephemerides (Winn et al. 2007; Pont et al. 2008) we determine that full occultation starts $\sim$13 exposures into O_3, and lasts for the remainder of this orbit. The effective exposure time for each spectrum was $T = 1.624$ s; the overall instrumental configuration, including the location of the spectrum on the focal plane array, was identical to that in SVT08. A few spectral calibration exposures (in O_1) were acquired using a narrow-band filter.

Because the NIC-3 camera is severely undersampled and because of large gain drop-off at the edges in the NICMOS detector pixels, the instrument was configured in DEFOCUS mode (full-width-at-half-maximum (FWHM) $\simeq 5$ pixels). This defocus reduces the level of photometric fluctuations due to both pointing jitter (random) and beam wander (systematic) errors. While the defocus also helps to minimize the bright-source overheads for this extremely bright target, it nevertheless limits the effective spectral resolution to $R \simeq 40$.

2.1. Data Analysis

A complete description of the data-analysis methods is provided in the supplementary information to SVT08. Herein, we discuss only departures and addenda to these analysis methods.

First, each image is reduced to a one-dimensional spectrum covering 1.5–2.5 μm in spectral range. This includes combining data from the grating's first and second orders, which are simultaneously imaged onto the detector array. Inclusion of the second order improves the signal-to-noise ratio (S/N) in the blue because the second order, which is partially imaged onto the detector, contains more detected photon flux at the shortest wavelengths (shortward of 1.7 μm, longward of which the efficiency of the second order falls rapidly) as a consequence of the peculiar blaze of the parent grating. Prior to combination, wavelength solutions for both orders were obtained using the calibration exposures and the wavelength-scale coefficients in Nicmoslook (Freudling et al. 1997). Merger of the spectral orders takes advantage of the near-integer ratio, $\simeq 2$, of the spectral resolutions of the two orders. The orders are coadded around a fiducial wavelength, and any smearing is captured by assigning the coadded channel a wavelength equivalent to
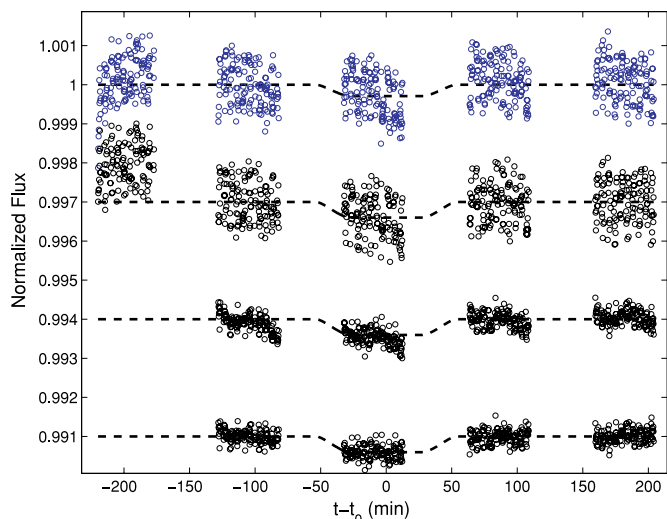
Figure 1. This figure shows a set of normalized light curves plotted against time (in minutes; t_0 corresponds to MJD 54220.1442888) in a top-to-bottom sequence. To aid the eye, we plot the data together with a set of model light curves calculated assuming a uniform disk for HD 189733b passing behind the parent star. (A) The top curve is a raw broadband or "white-light" light curve showing all five orbits. The small broadband eclipse depth of 2.9×10^{-4} is barely obvious in this light curve. (B) Next is a raw "red-broadband" light curve covering a wavelength range of 1.9–2.44 μm. The somewhat larger photometric depth of 4.1×10^{-4} is more easily discernible here. Orbit 1 data are poorly behaved over this restricted band. (C) Next is the "red-broadband" light curve after the removal of point-to-point photometric correlations. This step tightens the scatter in the light curve. Note that temporal correlations are not removed and are clearly seen in the light curve. (D) At the bottom is a fully processed light curve with all correlations modeled and removed. Gaps in the time series occur because HD 189733 is not in the continuous viewing zone for the *HST*.
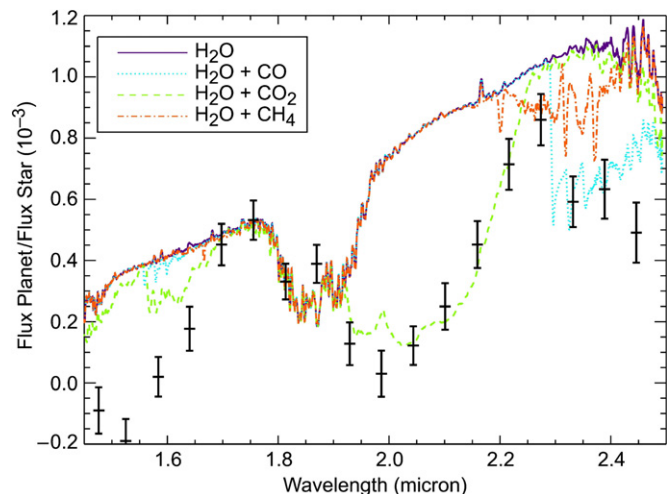
Figure 3. The near-IR dayside emergent spectrum used in our analysis with $\pm 1 - \sigma$ errors shown (black), together with a model spectrum (orange) containing the molecules H_2O, CO, CH_4, and CO_2, which are responsible for the absorption features (the strongest of which are identified above). The model also includes H_2-H_2, which contributes continuum opacity. The fit residuals suggest that one or more additional molecular species may be present. Although the fit is improved slightly by including C_2H_2, C_2H_6, or NH_3, additional data are required to make a strong case for the presence of additional molecular species.

Figure 2. A comparison of the observed spectrum (black markers with error bars) to a sequence of component models showing the effect of water together with individual carbon-bearing molecules included in our final model. This comparison shows the portion of the spectrum where each molecule has significant opacity. In particular, the role of CO_2 in producing the observed minima between 1.95 and 2.15 μm is evident.

the weighted average of wavelengths of component channels. Prior to coadding, the second-order spectra were multiplied by a broad Tukey window so as to suppress the effects of (1) the sharp band-edge at 1.5 μm and (2) the detector array edge at $\sim 1.85\,\mu$m on the final spectrophotometry. Lastly, coadded spectra are rebinned to wavelength channels at the binwidth of the DEFOCUS FWHM, guaranteeing adjacent channels have independent spectral content. As the state variables are
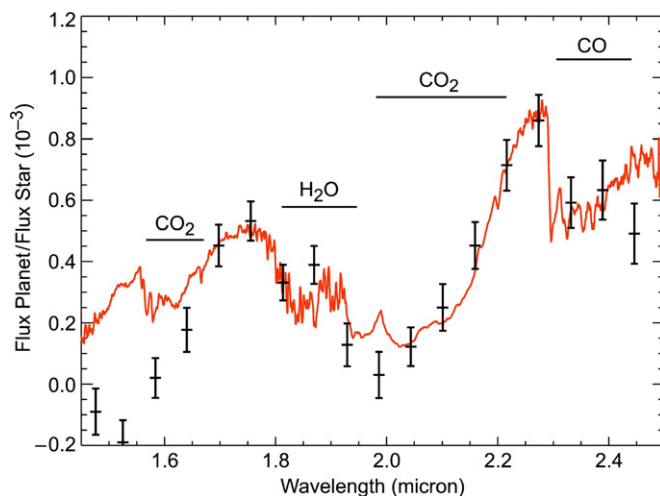
channel independent, the two orders can be coadded prior to decorrelation (see below). The secondary eclipse is observable in the raw light curves (see Figure 1) and especially so in spectral subbands with high contrast (e.g., around 2.3 μm; see Figure 3). For example, if we divide the "red broadband" (see the caption to Figure 1) into two subbands between 1.9–2.2 μm and 2.2–2.5 μm, little contrast is apparent in the former while a large contrast is seen in the latter.

The nature of the state variables chosen for decorrelation has been discussed extensively in SVT08-SI. One change is in the array temperature vector: instead of using temperatures from the probe at the NIC-1 mounting cup, we use the diode properties of the detector pixels as proxy for the detector temperature because the measurable detector bias voltage is highly temperature sensitive. These temperatures were extracted by the STScI staff on request (courtesy N. Pirzkal 2008, private communication). We find that the peak-to-valley variations of the state variables are similar (i.e., < 0.1 pixel for PSF displacement) to those seen in the observations of SVT08 for all orbits included in the fitting procedure, i.e., $O_2 - O_5$. A large rotation of the dispersion axis is apparent in O_1, and O_1 data were discarded in order to satisfy our underlying assumption—that spectrophotometry systematics are linear in small perturbations of the state variables. After O_1 the rotation settles, although O_2 shows a larger rotation from mean than the final three orbits.

The framework for decorrelation of the light curves is the joint energy minimization procedure described in SVT08, i.e., modeling and removal of the systematics was performed simultaneously, with the eclipse depth, $\alpha(\lambda)$, left as a free variable. The unique χ^2 minima in the $\alpha - \lambda$ space determine the emission spectrum. The point-to-point photometric scatter (see Figure 1), which is stochastic in time but common to all wavelength channels, is estimated using optimally weighted fit-residuals as in SVT08-SI. For all channels, the final residual vectors are examined via Lomb–Scargle periodograms to ensure that correlated $1/f$ noise, as well as noise at the *HST* orbital period and its overtones, is removed. An alternative scheme that uses just the baseline light curves to fit for a model (SVT08-SI)

Wavelength (μm)	$F_{\text{planet}}/F_{\text{star}}$	Error
2.446	0.000491	0.00009
2.389	0.000633	0.00009
2.332	0.000592	0.00008
2.274	0.000860	0.00008
2.216	0.000714	0.00008
2.159	0.000452	0.00007
2.101	0.000250	0.00007
2.044	0.000122	0.00006
1.986	0.000030	0.00007
1.929	0.000128	0.00007
1.869	0.000389	0.00006
1.814	0.000331	0.00006
1.755	0.000532	0.00006
1.698	0.000452	0.00007
1.640	0.000177	0.00007
1.584	0.000021	0.00006
1.525	−0.000190	0.00007
1.476	−0.000089	0.00008

and then interpolates to determine the emission spectrum gave answers that were statistically consistent with the joint energy minimization scheme; this implies that just the baseline orbits provide an adequate model.

The importance of the various state variables in modeling the overall systematics is assessed via principal components. The model in each light curve is first decomposed along each state vector, which is converted to a channel-wise correlation matrix. Each correlation matrix is diagonalized, along with the computation of the principal vectors. We find that a maximum of two principal components is required to model the bulk of the variance in the channel light curves. The rotation $\hat{\theta}$ and the displacements $\hat{x}$, $\hat{y}$ are the most important projections onto the first principal component, which models between 55% and 90% of the variance across channels. The spacecraft orbital phase, $\hat{\phi}_H$, is the single most important projection onto the second principal component. This behavior is largely explained by the fact that most elements in the set of state vectors show some dependence on the spacecraft orbital period.

The final emission spectrum (planet/star ratio) is shown in Figures 2 and 3 and tabulated in Table 1. The error bars contain three major components in quadrature. These are as follows: (1) the random noise, including detection noise, errors in the estimation of the state vectors, and any remaining systematics are contained in the light-curve residuals, (2) stochastic uncertainties in the model are computed by bootstrapping, and (3) gross errors in the model fitting. The latter are estimated either via Monte Carlo methods by applying random perturbations to the model components (SVT08-SI), or via the χ^2 surfaces obtained from the fitting procedure. Finally, we draw attention to the fact that the penultimate bluest channel (1.525 μm) has an unphysical eclipse depth; specifically, the wavelength channel is negative at 2.5σ. This may be due to the fact that this channel contains a dead pixel in the brightest part of the spectral image. We have not evaluated the effect of such dead pixels on the spectrophotometry in a strict statistical sense; consequently, such effects are not reflected in the error bar for that channel. Previous ground-based observations have been used to estimate the K-band planet/star contrast upper limit as 0.00039 (Barnes et al. 2007). We find the contrast in the

same passband (averaging the contrast in our spectral channels between 1.98 and 2.38 μm) to be 0.0004; given the challenges associated with ground-based secondary eclipse measurements, we do not consider the difference significant.

3. DISCUSSION

The interpretation of emergent spectra is generally complex because molecular bands could appear either in emission, absorption, or both, depending on the detailed temperature, pressure, and chemical profile of the planetary atmosphere. Nonetheless, when molecular species with detectable spectral features are present, radiative-transfer models can be used to retrieve the temperature and abundance structure of the photosphere of emission. This approach, used extensively for the study of planetary atmospheres in our solar system (Goody & Yung 1989), is the basis of our spectral retrieval.

We undertook a detailed analysis using a line-by-line, radiative-transfer model developed for disk-averaged planetary spectra and subsequently adapted for the specific case of hot Jupiters (Tinetti et al. 2006, 2007b). The model covers a pressure range from $1 \leqslant P \leqslant 10^{-6}$ bar in which the individual model layers are populated by abundance profiles for molecules used in the retrieval process. The opacity contribution of each molecule is computed based on its mixing ratio c_i, local density (ρ), and temperature in accordance with the assumed $T - P$ profile. Our compendium of line lists is the same as that given in SVT08. Trial planetary spectra were converted to contrast spectra using an ATLAS-9 model spectrum of a K1–K2V star with solar abundances (Kurucz 1993). To retrieve molecular abundances and the temperature profile, we iteratively compared the modeled contrast spectra to the observed near-IR spectra as well as mid-IR *Spitzer*-IRAC photometry (Charbonneau et al. 2008). We found that the IRAC photometry did not provide constraints for molecular mixing ratios, although those data were consistent with a decreasing T profile. Thus, the results for molecular abundances presented here are independent of IRAC data that probe lower pressures in the atmosphere.

The significant spectral modulation present in the near-IR contrast spectrum is best explained by the presence of water vapor and the carbon-bearing molecules CO and CO_2. The model requires a decreasing temperature with altitude between $\simeq 1 < P < 10^{-2}$ bar (the relevant photosphere). The modeling began by including the minimum number of molecules (H_2O, CO, and CH_4) composed from the most abundant reactive elements (H, O, and C). These molecules are highly plausible; H_2O and CH_4 have already been inferred via transmission photometry and spectroscopy (Tinetti et al. 2007a; Swain et al. 2008), and CO, thermochemically the most stable carbon molecule on the hot dayside, has been inferred from photometry (Barman 2008; Charbonneau et al. 2008). However, this minimal combination of molecules is unable to reproduce the large contrast deficit in the 1.95–2.15 μm region of the spectrum, suggesting additional opacity by the 2 μm combination bands of CO_2. The inclusion of CO_2 in the model reproduces the major features of the observed spectrum. Figure 2 illustrates the contribution of individual molecules to the model spectrum; the significance of CO_2 is evident. This suggests searching for evidence of other CO_2 bands, such as the 15 μm band, which may be present in the *Spitzer* mid-IR spectra (Grillmair et al. 2007).

Although CO_2 is not the primary carrier of carbon in the pressure and temperature range of relevance here, it is thermochemically predicted to be fairly abundant (10^{-6} for

solar abundance) when CO is the major carbon-bearing gas (Lodders & Fegley 2002), and has been discussed in the context of low-gravity brown dwarf spectral models (Saumon et al. 2003; Mainzer et al. 2007). It is formed via the net thermochemical reaction

$$CO + H_2O \rightleftharpoons CO_2 + H_2.$$
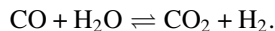
Additionally, CO_2 is readily produced by the reaction

$$CO + OH \rightleftharpoons CO_2 + H,$$
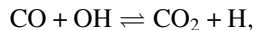
where the hydroxyl radical OH is derived from photolysis of H_2O (Liang et al. 2003).

While the observed spectrum places strong constraints on what major molecules are present, the model fitting must deal with a degeneracy between dT/dP and the molecular mixing ratio. In order to estimate the range of plausible mixing ratios for the inferred species, our final family of models explored a range of T profiles (Barman 2008; Burrows et al. 2008), with constant vertical mixing ratios for H_2O, CO, and CO_2, and a vertical mixing profile for CH_4, as derived by Liang et al. (2003). Based on this family of models, we find the following range for mixing ratios at the pressures and altitudes relevant here: H_2O ($c \sim 0.1 - 1 \times 10^{-4}$), CO ($c \sim 1 - 3 \times 10^{-4}$), CO_2 ($c \sim 0.1 - 1 \times 10^{-6}$), and CH_4 ($c \leqslant 1 \times 10^{-7}$). These values imply a $0.5 \leqslant C/O \leqslant 1$ together with a metallicity that is potentially subsolar. The inclusion of CO_2 in our models does not explain the contrast deficits at the band edges, particularly the blue edge at 1.6 μm (Figure 3). One possibility is the presence in the atmosphere of trace amounts of hydrocarbons such as acetylene (C_2H_2), ethane (C_2H_6), and possibly ammonia (NH_3). For example, C_2H_2, CH_4, and C_2H_6 can be produced via photolysis of CO (the primary reservoir for carbon) and water (Liang et al. 2004), while ammonia is likely to be found in low concentrations ($c \simeq 10^{-7}$) in thermal equilibrium with N_2, which is the dominant reservoir for nitrogen in these conditions. Indeed, including one or more of the above molecules does improve the model fit at the band edges. However, a firm assertion of their presence amongst a myriad of possibilities would require better data and/or broader wavelength coverage.

4. CONCLUSIONS

In summary, we have presented the first near-IR spectrum of light emitted by a hot-Jupiter-type planet. Using a radiative-transfer model, we determine that the molecules H_2O, CO, and CO_2 are likely present on the dayside of HD 189733b, and we are able to estimate abundances for these species. Although we cannot tightly constrain the slope of the temperature profile, the observed absorption features indicate that temperature decreases with altitude at pressures between 1 and 0.01 bar. In addition, there are residual features in the spectrum that could be explained by including opacities of other species that are presently not well constrained.

This work represents an initial step in exploiting the power of spectral analysis (even at low resolutions of $R \simeq 40$) in

determining the chemical composition of extrasolar planetary atmospheres; it also illustrates the extraordinary potential of the NICMOS instrument for characterizing bright, transiting exoplanets. In a previous paper, we presented a transmission spectrum of this planet at the terminator (SVT08), in which methane is seen to be more abundant ($c = 5 \times 10^{-5}$) in the higher, cooler regions of the terminator region atmosphere. However, it is difficult to compare directly the previous terminator results with our current dayside results because they probe atmospheric regions with significantly different temperatures and altitudes on this highly irradiated planet. The development of sophisticated global circulation and chemistry models could significantly advance the state of the art in this respect.

REFERENCES

Barman, T. 2008, ApJ, 676, L61
Barnes, J. R., et al. 2007, MNRAS, 382, 473
Bouchy, F., et al. 2005, A&A, 444, 15
Burrows, A., Budaj, J., & Hubeny, I. 2008, ApJ, 678, 1436
Charbonneau, D., et al. 2008, arXiv:0802.0845v1
Deming, D., Seager, S., Richardson, L. J., & Harrington, J. 2005, Nature, 434, 740
Fortney, J. J., Saumon, D., Marley, M. S., Lodders, K., & Freedman, R. S. 2006, ApJ, 642, 495
Freudling, W., Storrs, A., Pirzkal, N., & Pasquali, A. 1997, AAS, 191, 1002
Goody, R. M., & Yung, Y. L. 1989, Atmospheric Radiation (Oxford: Oxford Univ. Press)
Grillmair, C. J, Charbonneau, D., Burrows, A., Armus, L, Stauffer, J., Meadows, V., Van Cleve, J., & Levine, D. 2007, ApJ, 658, L115
Knutson, H. A., et al. 2007, Nature, 447, 183
Knutson, H. A., et al. 2008, arXiv0802.1705K
Kurucz, R. L. 1993, Kurucz CD-Rom, Atlas 9 (SAO, Cambridge)
Liang, Parkinson, C. D., Lee, A. Y.-T., Yung, Y. L., & Er, S. 2003, ApJ, 596, L247
Liang, M.-C., Seager, S., Parkinson, C. D., Lee, A. Y.-T., & Yung, Y. 2004, ApJ, 605, L61
Lodders, K., & Fegley, B. 2002, Icarus, 155, 393
Mainzer, A. K., Roellig, T. L., Saumon, D., Marley, M. S., Cushing, M. C., & Sloan, G. C. 2007, ApJ, 662, 1245
Pont, F., Knutson, H., Gilliland, R. L., Moutou, C., & Charbonneau, D. 2008, MNRAS, 385, 109
Saumon, D., Marley, M. S., & Lodders, K. 2003, arXiv:astro-ph/0310805
Showman, A. P., Cooper, C. S., Fortney, J. J., & Marley, M. S. 2008, ApJ, 682, 559S
Swain, M. R., Vasisht, G. V., & Tinetti, G. 2008, Nature, 452, 329
Tinetti, G., et al. 2006, Astrobiology 6, 34
Tinetti, G., et al. 2007a, ApJ, L99
Tinetti, G., et al. 2007b, Nature, 448, 169
Winn, J. N., et al. 2007, AJ, 133, 1828